



# Self-propulsion via slipping: Frictional swimming in multilegged locomotors

Baxi Chong<sup>a,b</sup> , Juntao He<sup>c</sup>, Shengkai Li<sup>b</sup> , Eva Erickson<sup>b</sup>, Kelimar Diaz<sup>a,b</sup>, Tianyu Wang<sup>c</sup> , Daniel Soto<sup>c</sup>, and Daniel I. Goldman<sup>a,b,c,1</sup>

Edited by Ruike Renee Zhao, Stanford University, Stanford, CA; received August 10, 2022; accepted January 25, 2023, by Editorial Board Member John A. Rogers

**Locomotion** is typically studied either in continuous media where bodies and legs experience forces generated by the flowing medium or on solid substrates dominated by friction. In the former, centralized whole-body coordination is believed to facilitate appropriate slipping through the medium for propulsion. In the latter, slip is often assumed minimal and thus avoided via decentralized control schemes. We find in laboratory experiments that terrestrial locomotion of a meter-scale multisegmented/legged robophysical model resembles undulatory fluid swimming. Experiments varying waves of leg stepping and body bending reveal how these parameters result in effective terrestrial locomotion despite seemingly ineffective isotropic frictional contacts. Dissipation dominates over inertial effects in this macroscopic-scaled regime, resulting in essentially geometric locomotion on land akin to microscopic-scale swimming in fluids. Theoretical analysis demonstrates that the high-dimensional multisegmented/legged dynamics can be simplified to a centralized low-dimensional model, which reveals an effective resistive force theory with an acquired viscous drag anisotropy. We extend our low-dimensional, geometric analysis to illustrate how body undulation can aid performance in non-flat obstacle-rich terrains and also use the scheme to quantitatively model how body undulation affects performance of biological centipede locomotion (the desert centipede *Scolopendra polymorpha*) moving at relatively high speeds ( $\sim 0.5$  body lengths/sec). Our results could facilitate control of multilegged robots in complex terradynamic scenarios.

locomotion | myriapod | slipping | drag anisotropy | frictional swimming

Locomotion by body undulation is common in both organisms and robots continuously immersed in an environment (such as fluids or granular media) (1–7). During such self-propulsion, body elements continuously experience forces set by the physics of the medium and the instantaneous orientations and velocities of body elements. An approach for analyzing such locomotion, which integrates thrust and drag forces over the body, was introduced in the early to mid-20th century and goes by resistive force theory (RFT). This method has successfully modeled organisms in highly damped hydrodynamic and granular terradynamic environments, like microorganisms, sand-swimmers, etc. (8–11). RFT works at its core because of a so-called “drag anisotropy” as elements translate through continuous media. For example, long thin systems like spermatozoa undulating in fluids can be thought of as a superposition of slender rods, which differ in reaction forces in the perpendicular and parallel directions (12–16).

In contrast, on solid terradynamic environments like flat ground, a key feature of the locomotion dynamics is that the anatomical elements (e.g., legs or body segments) are no longer in constant contact with the environment. Rather, these elements can make and break contact. Such time-varying contact enables effective locomotion for both legged (17, 18), limbless (e.g., sidewinding (19)), and peristaltic locomotion (20, 21). Interactions are typically assumed to be rate-independent isotropic Coulomb friction. In such situations, control algorithms (22, 23) have been developed to minimize slip\* during substrate contact; similarly, such active slip avoidance is also observed in biological systems (24, 25). Slipping is actively avoided partially because Coulomb friction introduces a step-function between the velocity-friction relationship, which can cause unstable oscillations (26). Furthermore, if not properly controlled, slipping can reduce the energetic efficiency of the locomotor (27).

While the bulk of prior work on terrestrial locomotors (28) focuses on systems with two or four legs, many biological systems, and increasingly robotic devices, possess

## Significance

Drag anisotropy is believed to be the critical principle which enables effective undulatory swimming in flowable media. Here, we show that undulatory locomotion with leg retraction/protraction can be recast as a fluid-like problem with the nonlinearities of foot-ground interactions leading to acquired drag anisotropy. In doing so, our framework allows for the comparison and cross-referencing of undulatory locomotion across diverse substrates. Further, from robophysical and biological experiments, we show that undulatory multilegged frictional swimming can be quantitatively described using a geometric model with low-dimensional centralized control framework. Our analysis not only facilitates the control of robust robot locomotion in complex terradynamic scenarios but also gives insight into neuromechanical control and the evolution of myriapod locomotion.

The authors declare no competing interest.

This article is a PNAS Direct Submission. R.R.Z. is a guest editor invited by the Editorial Board.

Copyright © 2023 the Author(s). Published by PNAS. This article is distributed under Creative Commons Attribution-NonCommercial-NoDerivatives License 4.0 (CC BY-NC-ND).

\*To whom correspondence may be addressed. Email: daniel.goldman@physics.gatech.edu.

This article contains supporting information online at <http://www.pnas.org/lookup/suppl/doi:10.1073/pnas.2213698120/-DCSupplemental>.

Published March 10, 2023.

multiple sets of legs (e.g., cockroaches have six, and centipedes can have up to 40 legs). In contrast to the few-legged systems in which an assumption of no-slip contact is often valid (29), for systems with more than four legs, there is a high likelihood that slip occurs during locomotion (30) because of kinematic constraint violations, e.g., the BigAnt (30). We hypothesize that, instead of avoiding slipping, multilegged locomotors can actively coordinate slips for effective propulsion, and we can analyze such behavior using a method similar to RFT in continuous media. Based on such insights, we further establish a unifying model for locomotion on both terrestrial and continuous media. The challenges in such unification lie in the nonlinearity and the isotropy of Coulomb friction in terrestrial environments in contrast to the linear, anisotropic viscous drag.

To briefly summarize and help guide the reader, in this paper, we investigate the slipping and thrust-generation mechanism in multilegged locomotors where both body undulation and leg retraction contribute to slipping and self-propulsion. Using a centipede-like robophysical model (31), we show that the steady-state terrestrial locomotion has a property of geometric locomotion (negligible inertial effects) even when operated at a high frequency on a low-friction substrate. We use RFT to study slipping in multilegged systems and propose a principle of “acquired drag anisotropy.” Specifically, by periodic lifting and landing of body appendages, the nonlinear and isotropic Coulomb friction experienced on each leg can be recast into a velocity-dependent drag, similar to that of organisms at a low Reynolds number; we refer to such dynamics as “frictional swimming.” In an effort to unify our proposed slip-driven mechanism and the conventional minimal-slipping mechanism, we establish a performance space of frictional swimming and discuss the relative advantage (e.g., robustness over obstacle-rich environments) of body-dominated (slip-driven) over leg-dominated (minimal slipping) frictional swimming by robophysical experiments. Finally, we use our scheme to analyze the locomotion of a biological multilegged system (centipedes) and reveal its slip-driven frictional swimming behavior. Similar to our theoretical analysis and robophysical experiments, we observe a smooth gait transition from leg-dominated to body-dominated locomotion as speed increases.

## Body Undulation

We utilize a robophysical modeling approach (32) to systematically study terrestrial locomotion. Specifically, we construct a multilegged robot consisting of repeated modules. Each module contains one pair of legs and one body connection. All combined, each module has three degrees of freedom (DoF): the shoulder lifting joint that controls the contact states of contralateral legs, the shoulder retraction joint that controls the fore/aft positions of leg movements, and the body bending joint that controls the lateral body undulation (33). The synchronization of these three DoF is generated using the extended Hildebrand framework (34) and *SI Appendix* which prescribe a leg-stepping wave and a body undulation wave, both propagating from head to rear. The amplitude of body undulation,  $\Theta_{body}$ , the amplitude of leg movement,  $\Theta_{leg}$ , and the spatial wave number,  $\xi$ , then uniquely prescribe the gait of the multilegged robot. Note that unless otherwise mentioned, we set  $\xi = 1$  throughout the paper.

As discussed in prior work, body undulation can play an important role in multilegged systems (34, 35). In Fig. 1C, we show the midline trajectory during undulatory locomotion of the multilegged robot ( $\Theta_{body} = \pi/3$ ,  $\Theta_{leg} = 0$ ,  $n = 6$ , and  $n$  is the number of modules). Depending on the relative magnitude of

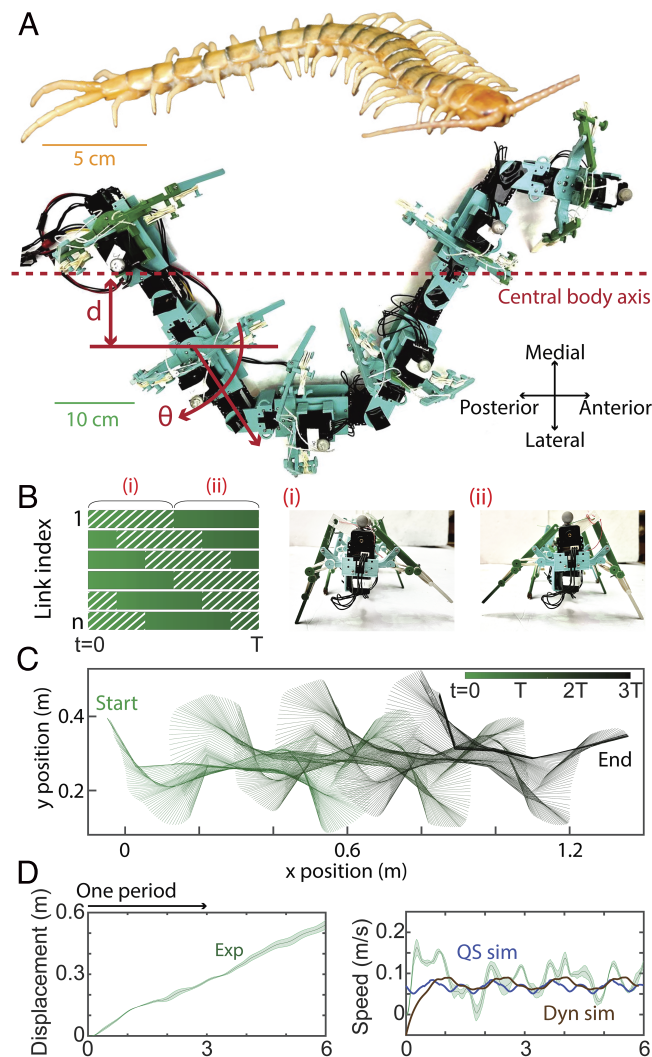


**Fig. 1.** Swimming in terrestrial environments. (A) Oblique view of the (Top) desert centipede, *S. polymorpha*, and (Bottom) an overhead view of the robophysical device. (B) (Left) Patterns of lifting and landing of contralateral feet. Each row represents the contact states of the  $i$ -th link. The shadow region represents the right foot in the stance phase, and the open region presents the left foot in the stance phase. (Right) Front view of the robophysical device lifting (i) left and (ii) right feet of the first module. (C) Trajectory of backbone during frictional swimming ( $\Theta_{body} = \pi/3$ ,  $\Theta_{leg} = 0$ ,  $n = 6$ ) colored by time. (D) (Left) Displacement and (Right) velocity profile of frictional swimming. We compare the experimental data with dynamical simulation (brown curve) and quasistatic simulation (blue curve) for body-dominated frictional swimming. After the transient development, both experiments' dynamical simulations converge to a limit cycle. After reaching steady state, average velocities are similar in experiments and simulation.

$\Theta_{body}$  and  $\Theta_{leg}$ , we broadly categorize the performance space into 1) body-dominated ( $\Theta_{body} \gg \Theta_{leg}$ ), 2) hybrid ( $\Theta_{body} \sim \Theta_{leg}$ ), and 3) leg-dominated ( $\Theta_{body} \ll \Theta_{leg}$ ). Although the body parts are lifted off the ground, we note that the undulatory body trajectory is similar to limbless undulatory motion commonly observed in snakes and nematodes locomoting in and on continuous media such as sand (36) and viscous fluids (37), respectively.

To quantitatively investigate frictional swimming, we track the trajectory of the center of geometry (CoG) of the robophysical model. In Fig. 1D, we illustrate the displacement and speed profile. Interestingly, we observe that after the transient response ( $t < 2s$ ) upon the initiation of the gait, the velocity trajectory converges to a limit cycle. To better understand the initial

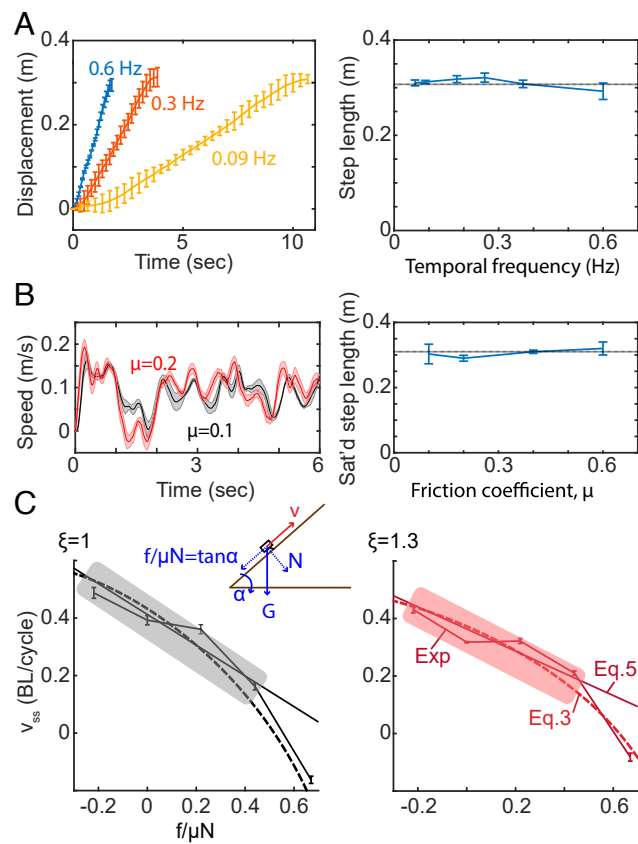


**Fig. 2.** The geometric nature of frictional swimming. (A) Robot ( $n = 6$ ) implementing the same gait ( $\Theta_{body} = \pi/3$ ,  $\Theta_{leg} = 0$ ) under different temporal frequencies. (Left) The development of CoG displacement as a function of time under different temporal frequencies. (Right) The step length (center of geometry, CoG, displacement per cycle) is stable over a range of temporal frequencies. Dashed lines represent prediction from quasistatic simulation. (B) Robot implementing the same gait on different substrates (different friction coefficients,  $\mu$ ). (Left) Development of CoG velocity as a function of time. Despite the initial high-magnitude oscillation, robots on low-friction surfaces converged to quasistatic velocity profiles after one gait cycle. (Right) The saturated step length is stable over a range of friction coefficients. (C) Experimental verification of force–velocity relationship ( $\Theta_{body} = \pi/3$ ,  $\Theta_{leg} = 0$ ,  $n = 8$ ). We test the relationship between the whole-body drag force and the velocity by measuring the step length of the robot on slopes. We compare experimental results (curves with error bar) and theoretical predictions from Eq. 3 (dashed curves) and 5 (solid curves) for two spatial wave numbers,  $\xi = 1$  and  $\xi = 1.3$ . In both experiments, we observe that there exists a linear relationship between force and velocity near equilibrium.

transient response and the limit cycle, we establish a dynamic model (*SI Appendix*) and a quasistatic model (34) (Fig. 1D). While the dynamic model underpredicts<sup>†</sup> the magnitude of the transient response upon the initiation of gait, the predicted velocity from this dynamic model also converges to a limit cycle. The average speed over a cycle is almost identical in experiments, the dynamic model prediction, and the quasistatic model prediction, indicating that inertial effects are not significant in the steady state of dynamic systems in frictional swimming.

To quantify the effect of inertia, we test the locomotion performance of the multilegged system ( $\Theta_{body} = \pi/3$ ,  $\Theta_{leg} = 0$ ,  $n = 6$ ) under different temporal frequencies (Fig. 2A). We show that, despite the changes in absolute speed (ranging from  $\approx 1.5$  cm/s to 15 cm/s), the step length (center of geometry (CoG), displacement per cycle with the units body lengths per

cycle (BL/cyc)) is almost constant. We empirically obtain the step length by measuring the distance between two consecutive foot–substrate contact points (intuitively: from touchdown to touchdown). Further, we test the locomotion performance of the multilegged system ( $\Theta_{body} = \pi/3$ ,  $\Theta_{leg} = 0$ ,  $n = 6$ ) on different surfaces ranging from coarsely fabricated wood ( $\mu \sim 0.6$ ) to coated smooth surfaces ( $\mu \sim 0.1$ ). Across all surfaces, the swimming motion converges to the steady-state equilibrium velocity within one gait cycle (Fig. 2B).

We posit that such convergence to steady-state equilibrium velocity is a result of emergent friction–velocity negative feedback. To explore this force–velocity relationship, we test the locomotion performance on slopes. Specifically, by varying the slope tilting angle  $\alpha$ , we measure the relationship between the external force,  $\tan \alpha$  (normalized by nominal friction  $\mu N$ ), and the step length. We test two undulatory gaits with different spatial wave numbers ( $\Theta_{body} = \pi/3$ ,  $\Theta_{leg} = 0$ ,  $n = 6$ ,  $\xi = \{1, 1.3\}$ ). In both cases, we observe a negative relationship (Fig. 2C) between external force and step length. The emergence of such a relationship not only explains the convergence (to steady-state locomotion) but also raises a nonintuitive concept: effective viscous drag emerges from frictional swimming with Coulomb friction. In the next sections, we will further analyze and model such effective viscous drag.

## Effective Viscous Drag

**Slipping Analysis.** Similar to locomotion at low Reynolds number, we consider frictional swimming as an undulatory swimming system but with assistance from periodic leg lifting and landing. As documented in prior work on locomotion at low Reynolds number (38, 39), the drag anisotropy of slender rods (higher reaction forces in the perpendicular than in the parallel direction) is the critical physical property enabling swimming in viscous flows. In terrestrial environments where drag force is typically assumed as isotropic Coulomb friction, the direct implementation of undulatory motion would be ineffective (40).

In Coulomb friction, the direction of ground reaction forces is opposite to the direction of slipping. Therefore, it is crucial to investigate the direction of slipping. Unlike other legged systems with fewer legs, there is significant slipping during undulatory locomotion of the multilegged robot. We predict from the quasistatic model that in body-dominated gaits, slipping is predominantly in the lateral direction. We verify this prediction by tracking the trajectory of the tip of a foot (second foot from the left) and empirically measuring the direction of slipping when operating a body-dominated gait ( $\Theta_{body} = \pi/3$ ,  $\Theta_{leg} = 0$ ,  $n = 6$ ). We quantify the direction of slipping by measuring the slipping angle  $\Psi$ , defined as the angle between the direction of slipping and the medial direction. We compare the experimentally measured and simulation-predicted time series of slipping angles in Fig. 3 A, ii, and both suggest that the direction of foot slipping is almost always perpendicular to the direction of motion ( $\Psi = 0$  or  $\pi$ ). Finally, we show the slipping angle profile from numerical simulation in Fig. 3 A, iii. We notice that for nearly all feet, the slipping angle is distributed around either 0 or  $\pi$ , both suggesting lateral/medial slipping.

The slipping profiles of other combinations of  $\Theta_{body}$  and  $\Theta_{leg}$  are shown in Fig. 3B and Fig. 4. We track the limb-slipping kinematics of three gaits (on flat terrain) with different combinations of  $\Theta_{body}$  and  $\Theta_{leg}$  for a 12-legged robot. We observe that the peak of  $\Psi$  shifts from anterior/posterior ( $\Psi = \pi/2 \pm \pi$ ) in leg-dominated gaits to lateral/medial ( $\Psi = 0 \pm \pi$ ) in body-

<sup>†</sup>We posit that it is the static friction that leads to the discrepancy between the empirically measured and model predicted transient response.

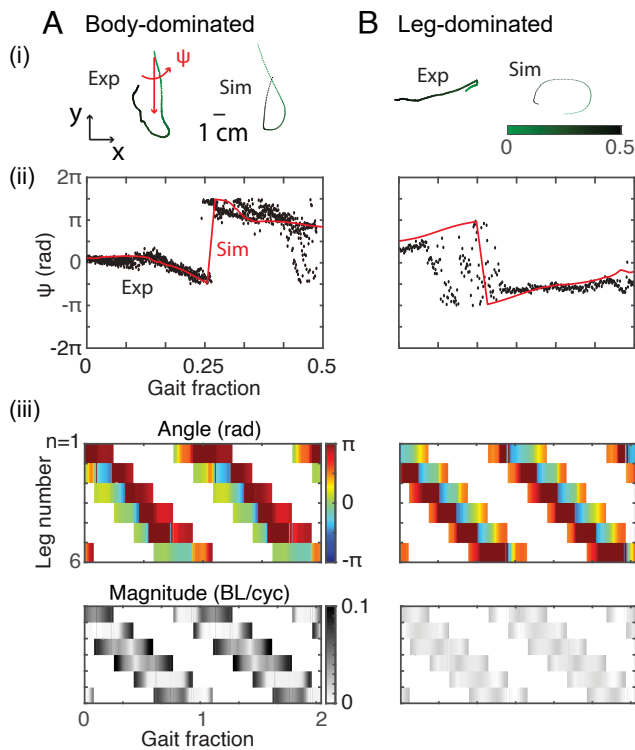


**Fig. 3.** Examples of limb-slipping kinematics in body-dominated and leg-dominated gaits. (i) Typical trajectories of a foot (second foot from the left) of a robophysical device (with 6 pairs of legs,  $n = 6$ ) during the stance phase for (A) body-dominated ( $\Theta_{body} = \pi/3$ ,  $\Theta_{leg} = 0$ ) and (B) leg-dominated ( $\Theta_{body} = 0$ ,  $\Theta_{leg} = \pi/6$ ) frictional swimming. The x-axis is the direction of motion. We quantify the slipping of a foot by its direction ( $\psi$ , units: rad) and magnitude (units: BL/cyc). (ii) Simulation prediction (red curves) and experimental measured (black dots) time series of slipping angles. (iii) Slipping profiles from simulation. We illustrate (Top) the slipping direction profile and (Bottom) the slipping magnitude profile.

dominated gaits (Fig. 4A). Further, we sample 20 points on the performance space and empirically calculate the slip rate. We quantify slip rate as the (slipping) distance in units of BL/cyc evaluated by the third leg from the left.

**Kinematic Model.** With the knowledge of lateral/medial dominated slipping, we develop a theoretical model to illustrate how periodic leg lifting and landing can acquire drag anisotropy similar to locomotors in viscous flow.

As documented in prior work on undulatory locomotion, each body segment experiences oscillation in the lateral and rotational direction with an offset of  $\pi/2$  (41, 42). Specifically,  $d$ , the distance from the body to the central body axis can be expressed as  $d(\tau) = d_m \sin \tau$ , where  $d_m$  is the magnitude of lateral oscillation and  $\tau \in [0, 2\pi]$  is the gait phase;  $\theta$ , the angle between the body orientation and the direction of motion can be expressed as  $\theta(\tau) = \theta_m \cos \tau$ , where  $\theta_m$  is the magnitude of rotational oscillation (Fig. 1A).  $\theta_m$  and  $d_m$  are determined by the amplitudes ( $\Theta_{leg}$  and  $\Theta_{body}$ ) and the spatial wave number ( $\xi$ ) of body undulation. From geometry, we know that  $d_m = n\Theta_{body}/(2\pi\xi)^2$ , and  $\theta_m = \Theta_{leg} + \tan^{-1}(n\Theta_{body}/(2\pi\xi))$ .

To simplify our analysis, we assume that the CoG of the robot has a constant forward velocity,  $v$ . The velocity of a foot on the right-hand side of body<sup>‡</sup> can then be expressed

<sup>‡</sup>For simplicity, we discuss only the right feet. The analysis of left feet will be symmetric to our analysis.

as a joint effect of CoG movement and the lateral/rotational oscillation:

$$\begin{aligned} v_x(\tau) &= \dot{d}(\tau) + l\dot{\theta}(\tau) \sin(\theta(\tau)) \\ v_y(\tau, v) &= v + l\dot{\theta}(\tau) \cos(\theta(\tau)), \end{aligned} \quad [1]$$

where  $v_x$  and  $v_y$  are velocity components in the lateral and anterior directions, respectively;  $l$  is the leg length. Friction acts in the opposite direction to the direction of foot slipping. Thus, the projection of the instantaneous frictional force to the anterior direction is

$$f_y(\tau, v) = -\mu N \sin \left( \tan^{-1} \left( \frac{v_y(\tau, v)}{v_x(\tau)} \right) \right), \quad [2]$$

where  $\mu N$  is the magnitude of the frictional force determined by the normal force  $N$  and the friction coefficient  $\mu$ . Assuming that each contralateral foot is in contact with the substrate for half of a period (e.g.,  $s_1 < \tau < s_1 + \pi$ ), we can calculate the average friction over the stance phase:

$$\bar{f}(v) = \int_{s_1}^{s_1+\pi} -\mu N \sin \left( \tan^{-1} \left( \frac{v_y(\tau, v)}{v_x(\tau)} \right) \right) d\tau. \quad [3]$$

Next, we can calculate the steady-state CoG velocity,  $v_{ss}$ , by assuming that the net force over a cycle is zero ( $\bar{f}(v_{ss}) = 0$ ). By the force balance,  $\bar{f}(v_{ss}) = 0$ , we establish an implicit function  $v_{ss} = v_{ss}(s_1)$ . Furthermore, we take a variational approach to find the optimal stance period [ $s_1, s_1 + \pi$ ] to maximize  $v_{ss}$  (i.e.,  $dv_{ss}/ds_1 = 0$ ). Note that the stance period is defined with respect to the phase of the local (leg) rotational and (body) lateral oscillations. Each leg has a distinct oscillation phase and therefore the distributions

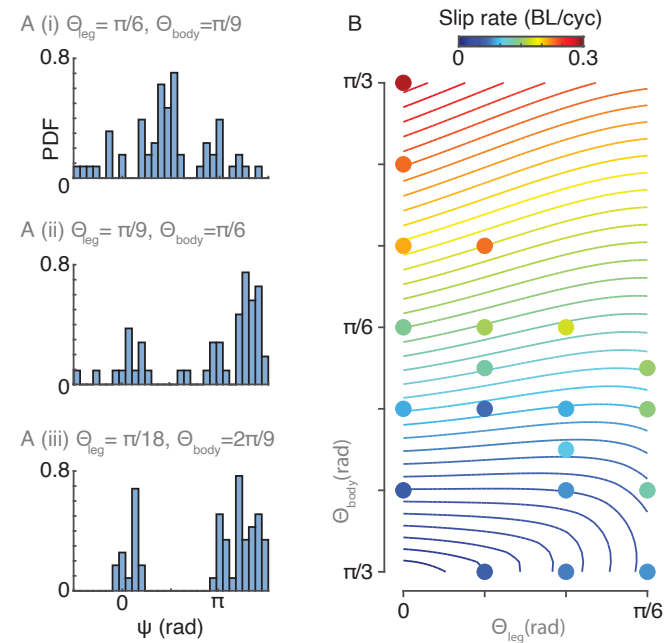


**Fig. 4.** Distribution of slipping direction and magnitude over different gaits. (A) Distribution of the leg-slipping direction  $\psi$  in the robophysical model for gaits with different combinations of  $\{\Theta_{leg}, \Theta_{body}\}$  (data from 3 trials for one gait). (B) The magnitude of slipping over the performance space. The underlying contour denotes model predictions. Circular markers (from 20 gaits chosen to span the performance space) represent empirical data by recording the slip rate in robophysical experiments (third leg from the left).

of stance periods are different across the many legs. The sufficient condition for  $s_1$  (to optimize  $v_{ss}$ ) is then

$$\sin \left( \tan^{-1} \left( \frac{v_y(s_1 + \pi)}{v_x(s_1 + \pi)} \right) \right) = \sin \left( \tan^{-1} \left( \frac{v_y(s_1)}{v_x(s_1)} \right) \right), \quad [4]$$

Solving Eq. 4 yields two optima:  $s_1 = 0$ ,  $s_1 = \pi$ . They correspond to maximal  $v_{ss}$  (highest forward speed) and minimal  $v_{ss}$  (highest backward speed), respectively. In other words, by properly controlling the sequence of lifting and landing, we can effectively acquire drag anisotropy in either direction and therefore enable swimming along (direct wave) and against (retrograde wave) the direction of wave propagation (43). Interestingly,  $s_1 = 0$  also optimizes body–leg coordination as reported in ref. 34 where the body undulation is considered to assist leg retraction. In this paper, we consider only retrograde-wave frictional swimming. Thus, we set  $s_1 = 0$  unless otherwise stated.

Since slipping is primarily in the lateral direction, we assume  $v_x \gg v_y$ . We can therefore calculate the changes in friction in response to a disturbance of the steady-state velocity ( $v = v_{ss} + \delta_v$ ):

$$f_y(\tau, v_{ss} + \delta_v) = -\mu N \sin \left( \tan^{-1} \left( \frac{\delta_v + v_y(\tau, v_{ss})}{v_x(\tau)} \right) \right)$$

$$[\because v_x \gg v_y] \approx f_y(\tau, v_{ss}) - \mu N \sin \left( \tan^{-1} \left( \frac{v_{ss}}{v_x(\tau)} \right) \right) \frac{\delta_v}{v_{ss}}.$$

Integrating over the stance period, we can obtain the changes of the average friction:

$$\underbrace{\bar{f}(v_{ss} + \delta_v)}_{\bar{f}_d(\delta_v)} = \underbrace{\bar{f}(v_{ss})}_{0} - \delta_v \int_0^\pi \underbrace{\frac{\mu N}{v_{ss}} \sin \left( \tan^{-1} \left( \frac{v_{ss}}{v_x(\tau)} \right) \right)}_{\gamma_0} d\tau$$

$$\bar{f}_d(\delta_v) = -\gamma_0 \delta_v. \quad [5]$$

The effective linear force–velocity relationship for a segmental interaction over a stance period allows the analysis of frictional swimming similar to that in viscous fluids. Further, Eq. 5 predicts that this equilibrium is asymptotically stable. Note that our analysis is invariant to the choice of foot. Eqs. 3 and 5 can thus be generalized to the overall multilegged system by a scaling factor of  $n$ . To verify our analysis, we compare predictions from Eq. 3 to Eq. 5 to the experimental measurement in Fig. 2C, and we observe good agreement between theory and experiments, especially locally near equilibrium.

## Performance Space

As discussed earlier, both body undulation and leg retraction can contribute to thrust generation in multilegged systems. To systematically explore the coordination and balance of body and legs, we introduce a “performance space” (Fig. 5) where the axes are  $\Theta_{body}$  and  $\Theta_{leg}$ . Note that competition exists between high  $\Theta_{body}$  and high  $\Theta_{leg}$  since it will lead to self-collision among legs, which can damage the robot. In previous discussions, we focused on the body-dominated frictional swimming regime of the performance space. The conventional leg-dominated counterpart experiments ( $\Theta_{body} = \pi/3$ ,  $\Theta_{leg} = 0$ ,  $n = 6$ ) are provided in Fig. 3B. We further illustrate the experimentally measured distribution of slipping metrics over different combinations of  $\Theta_{body}$  and high  $\Theta_{leg}$  in Fig. 4. Note that slipping in conventional leg-dominated gaits is significantly lower than those in body-dominated frictional swimming.

To study how speed is affected by gait (e.g., points in the performance space) and morphology (e.g., number of legs), we experimentally tested the locomotion performance on robophysical models with varying  $\Theta_{body}$ ,  $\Theta_{leg}$ , and  $n$ . Fig. 5A shows a heat contour of step length over performance space for robots with 4 (Fig. 5A, Left) and 8 (Fig. 5A, Right) pairs of legs. Here,

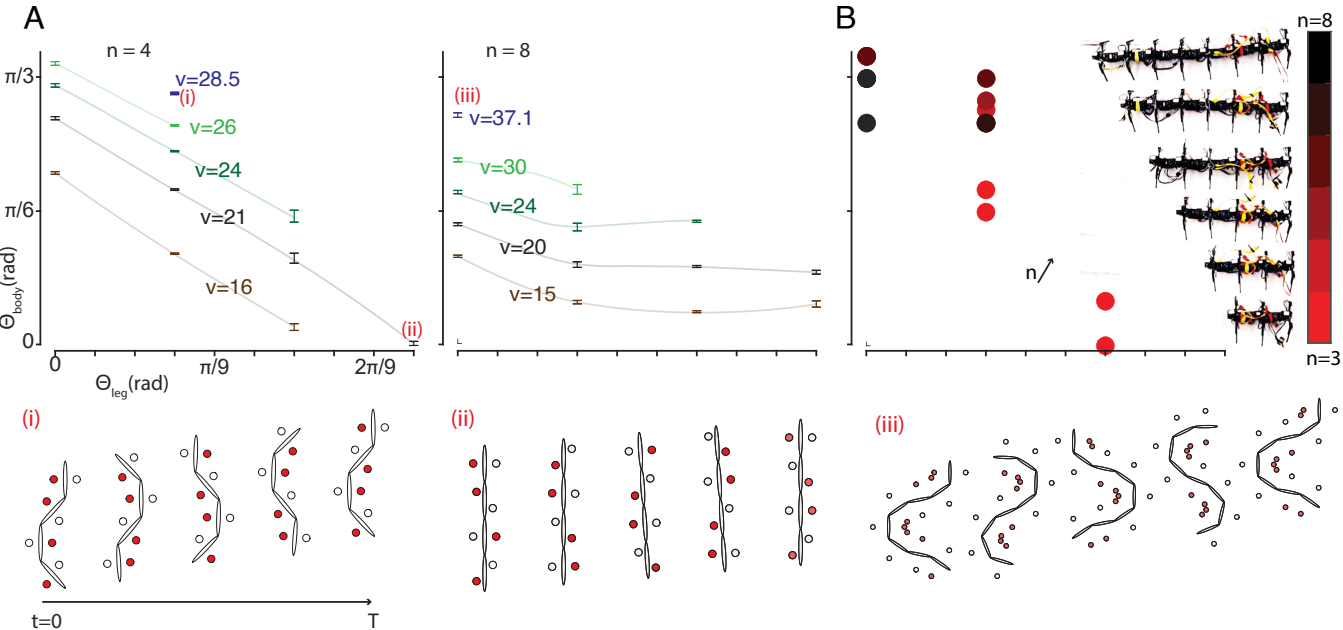


**Fig. 5.** Performance space of multilegged frictional swimming. We characterize body and leg driven locomotion using a performance space consisting of the amplitudes of body undulation and leg movement. (A) The heat contour of velocity ( $v$ , units: cm/cyc) over the performance space for a robophysical model with (Left) 4, (Right) 8 pairs of legs.  $n$  is the number of leg pairs. Note that optimal locomotion (the highest velocity) occurs at the “hybrid” region when  $n = 4$  and at body-dominated region when  $n = 8$ . (Bottom) Snapshots of body configurations over one cycle for (i)  $n = 4$ ,  $\Theta_{body} = 60^\circ$ ,  $\Theta_{leg} = 15^\circ$ , (ii)  $n = 4$ ,  $\Theta_{body} = 0^\circ$ ,  $\Theta_{leg} = 45^\circ$ , and (iii)  $n = 8$ ,  $\Theta_{body} = 60^\circ$ ,  $\Theta_{leg} = 0^\circ$ . (B) Transition of optimal terrestrial locomotion from leg-dominated to body-dominated as the number of leg pairs increases.

we fix the step frequency to 0.05 Hz. We notice that for systems with different leg pairs, the optima reside in different regimes. For robots with 4 pairs of legs, a hybrid mode of body undulation and leg retraction leads to the highest step length. On the other hand, for robots with 8 pairs of legs, pure body-dominated frictional swimming ( $\Theta_{leg} = 0$ ) leads to the highest step length. This is also evident in the gradient of isoheight contours. To further quantify the transition, we identify<sup>§</sup> the optima,  $[\Theta_{leg}, \Theta_{body}]$ , for robots with 3 to 8 pairs of legs. We then color the optima  $[\Theta_{leg}, \Theta_{body}]$  by  $n$ . From Fig. 5B, we observe that the optimum transitions from leg-dominated to body-dominated as the number of leg pairs increases.

From our model, we predict that the direction of slipping transitions from anterior/posterior in leg-dominated gaits to lateral/medial in body-dominated gaits, in agreement with our observations in robophysical experiments (Fig. 4). Further, the slip rate is significantly higher in body-dominated gaits than leg-dominated gaits. We calculate the distribution of slip rate over the performance space (underlying contours in Fig. 4). The empirical slip rate is in good agreement with model predictions.

## Interaction with Obstacles

In this section, we explore the relative advantages of body-dominated and leg-dominated gaits in obstacle-rich environments. We posit that the slipping direction plays an important role in the interaction with obstacles and that body-dominated gaits (with lateral/medial slipping) are more robust over the presence of obstacles as compared to leg-dominated gaits (with anterior/posterior slipping).

In Figs. 3 and 4, we compare the direction of slipping for leg-dominated and body-dominated gaits. Specifically, slipping in leg-dominated gaits almost always occurs first in the anterior direction and then follows in the posterior direction. This chronological order of slipping can affect the interaction with terrain heterogeneity (obstacles). In other words, the interaction between a leg and an obstacle is more likely to occur during the preceding slipping event than the succeeding slip. The presence of obstacles can interfere with slipping by introducing a reaction force opposite to the direction of slipping. Thus, the preceding anterior slipping feet in conventional leg-dominated gaits can be detrimental to locomotion. On the other hand, in body-dominated gaits, feet slip in lateral/medial directions in which reactions from interactions with obstacles are also in medial/lateral direction and will not affect locomotion performance in the direction of motion.

To verify this prediction, we construct a heterogeneous environment (low-height obstacles randomly distributed on a flat terrain (*SI Appendix*)) and test the locomotion performance of different gaits in the multilegged system ( $n = 6$ ). We identify three isoheight lines on the performance space such that all points on an isoheight line have the same step length on homogeneous environment. We choose the isoheight lines with  $v = 12$ ,  $v = 16$ , and  $v = 18$  (in units of cm per cycle, cm/cyc). We quantify the degree of body and leg use by the angle  $\beta = \tan^{-1} \left( \frac{\Theta_{leg}}{\Theta_{body}} \right)$ . Interestingly, we notice that gaits with higher  $\beta$  have significantly reduced step length in heterogeneous environments than in homogeneous environments.

To better understand the robustness of gaits in heterogeneous environments, we establish a statistical model of the locomotion

dynamics. To simplify the analysis, we approximate the slipping angle  $\Psi$  (Fig. 3) by  $\beta$  such that  $\Psi = 0$  during body-dominated frictional swimming ( $\beta = 0$ ) and  $\Psi = \pi/2$  during conventional leg-dominated frictional swimming ( $\beta = \pi/2$ ). Assuming that the reaction force from terrain heterogeneity,  $F$ , is constant, the projection of reaction force in fore-aft direction can be approximated by  $F \sin(\beta)$ . Consider an obstacle-rich environment with obstacle density  $\rho$  and a robot with  $n$  pairs of legs; then the distribution function of at least one leg interacting with an obstacle is  $h(y) = \{1 \text{ if } y < np; 0 \text{ if } y \geq np\}$ , where  $y \sim U(0, 1)$ ,  $U$  is the uniform distribution. Thus, the distribution function of the projection of reaction force in fore-aft direction is  $Fh(y) \sin(\beta)$ . From Eq. 5, the distribution function of step length is

$$\begin{aligned} v &\sim v_{ss} - \gamma_0^{-1} F \sin(\beta) h(y) \\ \bar{v} &= v_{ss} - \gamma_0^{-1} F(1 - n\rho) \sin(\beta) \\ \text{std}(v) &= \gamma_0^{-1} F \sqrt{n\rho(1 - n\rho)} \sin(\beta), \end{aligned} \quad [6]$$

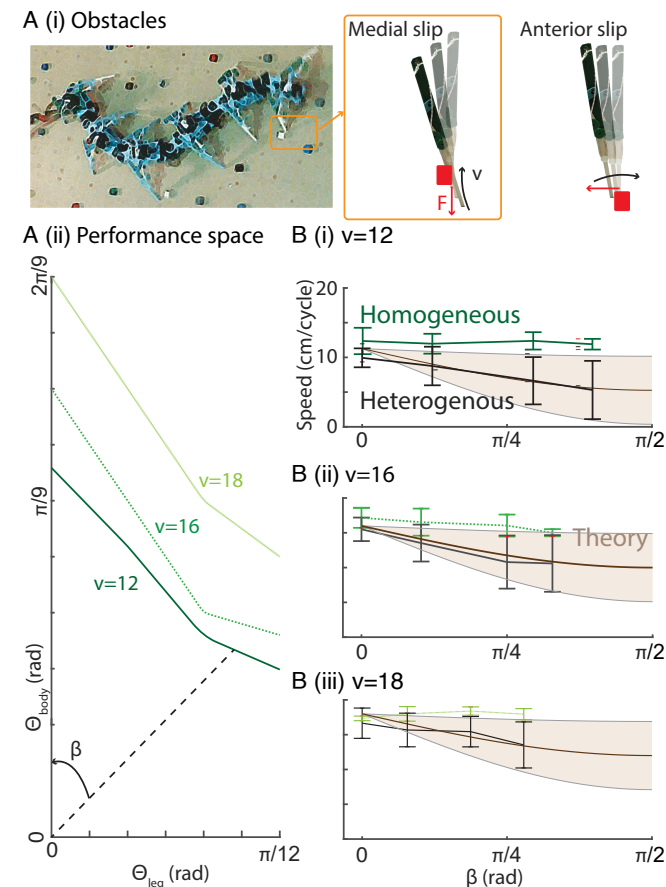


**Fig. 6.** Advantages of body-dominated frictional swimming in obstacle-rich environments. (A) (i) A snapshot of the robot ( $n = 6$ ) moving on obstacle-rich environments ( $\rho = 0.06$ ). Cartoon illustration of the interaction between robot and obstacles subject to different slipping directions (*Top*: typical body-dominated; *Bottom*: typical leg-dominated). Red blocks represent obstacles; legs from darker color to lighter color represent progression of time. (ii) We choose three theoretically predicted isoheight lines on the velocity heat contour over the performance space:  $v = 12$  cm/cyc,  $v = 16$  cm/cyc, and  $v = 18$  cm/cyc. We quantify the degree of body and leg use by  $\beta = \tan^{-1} (\Theta_{leg}/\Theta_{body})$ . (B) Comparison of locomotion performance in homogeneous (curves with error bar in green colors), heterogeneous environments (curves with error bar in black color), and theoretical predictions from Eq. 6 (curves and areas in light brown color). From *Top* to *Bottom*, the flat line descended from isoheight lines with  $v = 12$  cm/cyc,  $v = 16$  cm/cyc, and  $v = 18$  cm/cyc.

<sup>§</sup>For each robot, we first identify the gait with the highest average step length as the seed-optimal gait. We also consider a gait as one of the optima if there is no statistically significant difference between the seed-optimal gait.

where  $\gamma_0$  is the effective drag coefficient from Eq. 5. We observe quantitative agreement between the theoretical prediction and the experiments (Fig. 6).

## Biological Centipedes

Biological centipedes coordinate their body and leg movement to rapidly traverse different terrestrial environments (43–46). However, there has been limited biomechanical analysis on centipede locomotion. One of the challenges in analyzing centipede locomotion lies in the proper dimensionality reduction over the large number of legs and body segments. Despite recent efforts in dimensionality reduction in multilegged robots (31), it remains unclear whether such dimensionality reduction can be extended to biological centipedes. However, if identified, such a low-dimensional representation of centipede kinematics could pave the way toward developing centralized neuromechanical control hypotheses. Further, existing work on centipedes typically assumes that there is no foot slipping (47–49). Given the importance of slipping as illustrated in our robophysical experiments, we posit that slipping also plays an important role in biological centipede locomotion despite the seemingly low slip magnitude.

To gain insights into such issues, we use our low-dimensional slipping model to study rapidly-moving biological centipedes (Fig. 7A). We predict from our slipping analysis (solving Eq. 3) that body-dominated gaits should be a faster mode (greater step length) of locomotion as compared to leg-dominated. To test this prediction, we study the locomotion performance of a biological centipede (*Scolopendra polymorpha*) and characterize the leg dynamics under different speeds. Specifically, we collect high-speed video recordings of centipedes moving on a low-friction surface (white marker board,  $25 \times 10$  cm). We notice that the wave propagation in both body and leg has negligible variance in

the maximum amplitude (Fig. 7C), which allows us to represent the whole-body kinematics using a low-dimensional performance space consisting of body and leg amplitudes. Similar to our analysis on the robot, we compare a body-dominated gait (Fig. 7 A, i) and a leg-dominated gait (Fig. 7 A, ii) in biological centipedes and investigate the direction of foot slipping for both cases. Interestingly, we observe that slipping is prevalent and occurs mostly in the lateral/medial direction for body-dominated gaits. In contrast, the magnitude of slipping is reduced with slipping direction in anterior/posterior direction for leg-dominated gaits. Finally, we show the displacement and velocity profile for both body-dominated and leg-dominated gaits in Fig. 7B. Notably, our low-dimensional quasistatic model can give a quantitative prediction of the velocity profile for the relatively high-speed ( $\sim 0.5$  body lengths per second, BL/s) centipede frictional swimming, indicating a low-dimensional centralized control scheme in the seemingly complicated multilegged systems.

We extract the amplitude of body undulation ( $\Theta_{body}$ ) and leg movements ( $\Theta_{leg}$ ), the speed (in units of BL/s), and the step length (in units of BL/cyc) from each trial (6 individuals over 14 trials<sup>5</sup>). We note that speed correlates with both stepping frequency (Fig. 8 B, i,  $\rho = 0.77$ ,  $P < 0.01$ ) and step length (Fig. 8 B, ii,  $\rho = 0.79$ ,  $P < 0.01$ ), indicating that centipedes simultaneously increase their stepping frequency and step length to achieve higher absolute speeds. We proceed to investigate how centipedes modulate gaits to achieve higher step length. We illustrate the changes in  $\Theta_{leg}$  and  $\Theta_{body}$  as step length increases (Fig. 8 A, i, color denotes step length). As documented in prior work (43), we also observe the emergence of body undulation at higher speeds. Interestingly, we notice that the emergence of body undulation is accompanied by a decrease in  $\Theta_{leg}$ . This indicates that, in response to high speeds, there is a transition from leg-dominated gaits (high  $\Theta_{leg}$ , low  $\Theta_{body}$ ) to body-dominated gaits (low  $\Theta_{leg}$ , high  $\Theta_{body}$ ), in agreement with our prediction.

Given the significant slipping observed in both robophysical and biological experiments, we wonder how slipping affects energetic efficiency during locomotion. Thus, we next estimate the rate of mechanical energy dissipation during frictional swimming. In the Coulomb friction model, the magnitude of friction is independent of the magnitude of slipping velocity. We thus have  $\vec{f}(\tau) = [f_x(\tau), f_y(\tau)] = \mu mg \frac{\vec{v}(\tau)}{|\vec{v}(\tau)|}$ , where  $\vec{f}(\tau)$  and  $\vec{v}(\tau)$  are instantaneous frictional force and slipping velocity at  $\tau$  of a leg, respectively. From these relations, we can calculate the instantaneous power as  $P(\tau) = \vec{f}(\tau) \cdot \vec{v}(\tau) = \mu mg |\vec{v}(\tau)|$ . The energy dissipation per cycle is calculated as  $E = \int_0^\pi P(\tau) d\tau = \mu mg d_s$ , where  $d_s = \int_0^\pi |\vec{v}(\tau)| d\tau$  is the total slipping distance. Therefore, the amount of slipping can serve to quantify the mechanical energy dissipation. Here, we define the slip rate as the amount of slipping per cycle (in units of BL/cyc). In principle, the slip rate of all legs is identical. However, given the variation in leg length, amplitude of body undulation, and amplitude of leg movement, slip rate can also vary between legs. To keep our analysis consistent and reduce variation among individual legs, we choose the third leg from the left to approximate slip rate in centipedes. In Fig. 8 A, ii, we illustrate the changes in slip rate (denoted by color) in response to gait modulation.

We define slipping efficiency as the speed normalized by slip rate:  $\zeta = \frac{\text{step length}}{\text{slip rate}}$ . Note that the mechanical cost of transport (mCoT) is typically defined (50) as  $\text{mCoT} = \frac{\text{Energy cost}}{\text{Displacement} \times \text{mass}}$ .

<sup>5</sup>We choose trials where animals exhibited steady-state forward locomotion and are away from the walls.

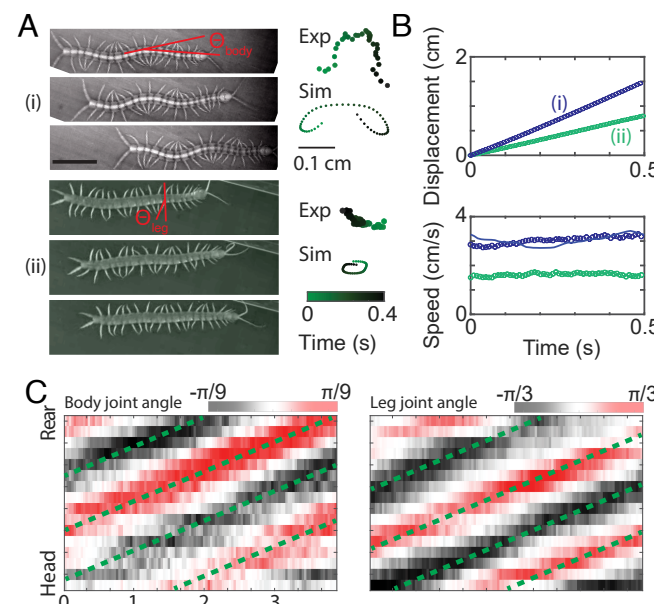


**Fig. 7.** Analysis of centipede locomotion on flat frictional surfaces. (A) (Left) Snapshots of a trial of (i) body-dominated and (ii) leg-dominated centipede locomotion. (Right) The trajectory of foot slipping colored by time. The stance phase spans 0.4 s. Trajectory of centipede body during frictional swimming colored by time. (B) The (Top) displacement and (Bottom) velocity profiles. Animal data are presented in circles, and the prediction from the quasistatic model is presented in the blue curve. (C) (Left) Body undulation and (Right) leg movement profile. The dashed green curve labels the propagation of the body wave and leg wave along the body. Axes are identical in all panels.

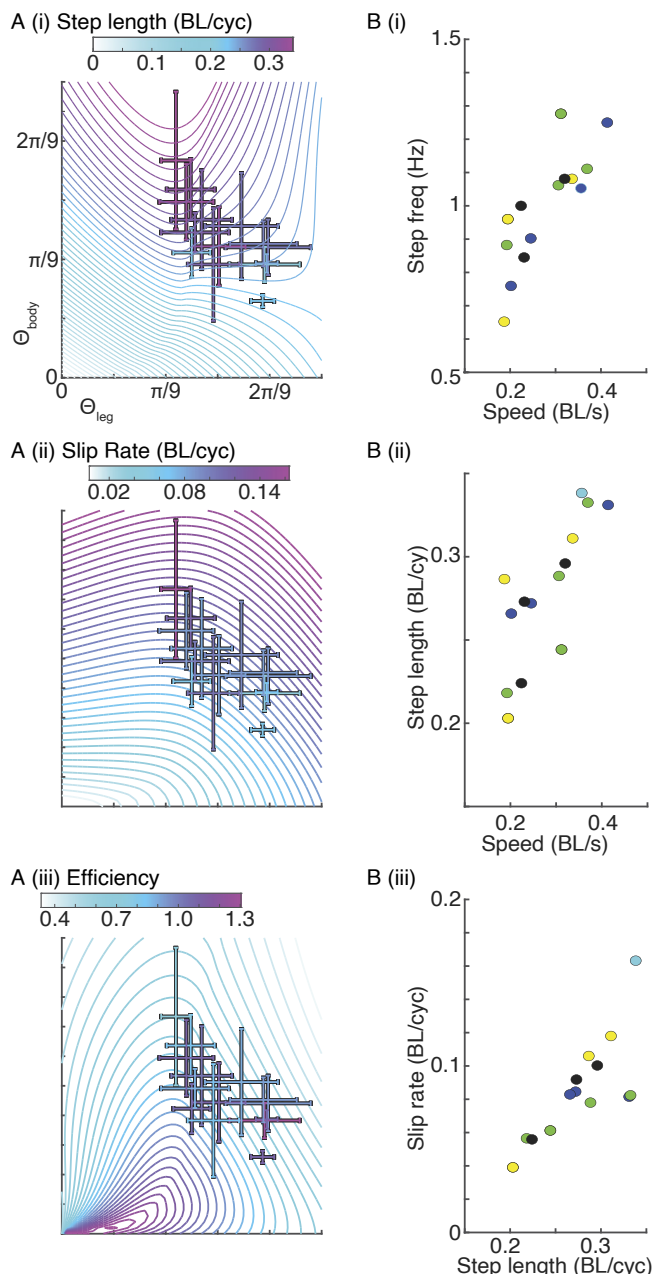


**Fig. 8.** Quantities associated with slip-driven centipede locomotion in the performance space. (A) (i) The distribution of body amplitude ( $\Theta_{body}$ ) and leg amplitude ( $\Theta_{leg}$ ) for centipede locomotion over a range of speeds. In each trial, we extract  $\Theta_{body}$  and  $\Theta_{leg}$  and represent it as a cross (colored by its step length) on the performance space. (ii) Distribution of slip rate for centipede locomotion over a range of speeds. Colors denote the slip rate (amount of slip per cycle measured from the third leg on the left). (iii) Distribution of efficiency for centipede locomotion over a range of speeds. Colors denote the efficiency (step length normalized by slip rate). Axes in (ii) and (iii) are identical to (i). The underlying contours denote model predictions. (B) Correlation (i) between speed and stepping frequency ( $\rho = 0.82, P < 0.01$ ), (ii) between speed and step length ( $\rho = 0.79, P < 0.01$ ), and (iii) between slip rate and step length from measured animal data ( $\rho = 0.77, P < 0.01$ ). In (B), color denotes data from five different individuals.

In this way, we can relate mCoT to the efficiency:  $mCoT = \mu/\zeta$ . In Fig. 8 A, iii, we estimate the slipping efficiency in centipedes. Interestingly, we observe that as speed increases, centipedes transition from low-step-length and high-efficiency gaits to high-step-length and low-efficiency gaits. Specifically, high-speed gaits are associated with high slip, as predicted from our model and

robophysical experiments. To illustrate this, we plot the measured slip rate and step length in animal data and observed a good correlation ( $\rho = 0.77, P < 0.01$ , Fig. 8 B, iii).

## Conclusions

In this paper, we performed systematic locomotion tests of a multilegged robophysical model on rigid frictional ground and found that its dynamics were highly damped, resembling those of microscopic swimmers at low Reynolds number. We then developed a theory to explain these observations and further used this theory to quantitatively model the locomotion of biological centipedes.

From a physics of locomotion perspective, this paper reveals that a unified framework can capture and explain undulatory swimming in highly damped environments with both intrinsic and acquired drag anisotropy. Drag anisotropy is understood to be the critical principle which enables effective undulatory swimming (38–40, 51, 52). Prior work has typically considered the intrinsic property of an element translating through a flowable medium (e.g., viscous fluid (38) and granular media (11, 53)) or a locomotors' surface structures (54, 55) as the cause of drag anisotropy and thus, effective undulatory swimming (51, 53, 56–58). More recently, studies have demonstrated effective undulatory swimming with no intrinsic drag anisotropy. These works modulated the magnitude of surface traction via either static friction (39, 40) or periodic lifting and landing of body appendages (34) to produce undulatory locomotion. Here, we posit that effective undulatory swimming shares the same physical principles between these two scenarios (intrinsic drag anisotropy and friction modulation). Specifically, we demonstrated that terrestrial multilegged locomotion can be recast as a fluid-like problem with the nonlinearities of the foot–ground interaction leading to acquired drag anisotropy in the environments dominated by isotropic, rate-independent Coulomb friction. Notably, the body–leg coordination to optimize leg retraction converges to the leg use to maximize acquired drag anisotropy. By performing these experiments and developing this framework, we broaden and deepen our understanding of undulatory swimming and allow for comparison and cross-referencing of locomotion in different substrates.

Our study further reveals the geometric nature of frictional swimming. Typically observed in highly damped environments, geometric locomotion has a property that net translation is generated from properly coordinated self-deformation to counter drag forces (59–62). During the last decades, physicists and engineers have developed a powerful geometric mechanics framework to understand biological undulatory swimming behaviors (31, 36, 42) and design novel swimming gaits for robots (62–64). This geometric approach replaces laborious calculation with illustrative diagrams and therefore offers quantitative and qualitative insights into locomotion. However, the application of geometric mechanics was limited to environments where friction dominated over inertial forces. Surprisingly, recent work successfully used geometric mechanics to study multilegged systems (30, 33, 34) despite not having a solid theoretical foundation (non-negligible inertia). Here, we showed that frictional swimming has a property of effective viscous drag, which guarantees the convergence to steady-state quasistatic locomotion despite changes in the temporal frequency and friction coefficient. In this way, our framework rationalizes the application of geometric mechanics to multilegged frictional swimming, offering building blocks for future exploration of frictional swimming using geometric mechanics.

From an engineering perspective, our robophysical studies and RFT scheme can aid in the development of multisegmented legged robots. If properly controlled, robots with different body morphologies and leg numbers could be used in different tasks. For example, legged robots are known for their agility (65–67), whereas multisegmented limbless (e.g., serially connected) robots for interactions with obstacles (68–70). Multisegmented legged robots have the potential to leverage the advantages of both multisegmented limbless and legged robots (71). However, to date, there has been no effective tool to control such devices to the full measure of their potential. With the help of our RFT framework and robophysical systematic experiments, our scheme paves the way toward an alternative for robust and agile locomotion.

Finally, our work can also contribute to an understanding of the neuromechanics of biological myriapod locomotion. With redundant legs, biological centipedes possess high mobility in diverse environments (43, 44, 48). Additionally, some centipedes are reported to display body undulation at high speeds (43, 44). Manton hypothesized that the use of body undulation is passive and thus detrimental to locomotion efficiency (43). In this way, Manton further posited that centipedes with the capability to resist body undulation at high speeds are neuromechanically advanced (43). Over the past century, the mechanism of body undulation has remained controversial. Using body-mechanical dynamic modeling, recent work (49, 72) suggested that the presence of body undulation could be a passive outcome of dynamic instability. On the contrary, electromyography (EMG) data analysis suggests that activity of the axial musculature causes body undulations, indicating an active nature of body undulation (44). Independent of a passive or active mechanism, the role (e.g., whether beneficial/detrimental) of body undulation during locomotion remains less studied. Here, our observation and analysis indicate that there exists a transition from low-step-length gaits to high-step-length gaits as speed increases, and such transition includes two essential steps: the emergence of body undulation and the reduction in leg amplitude. Thus, our model illustrates the essential role of body undulation to aid locomotion at high speed, offering insights into the neuromechanical and evolutionary studies of different centipedes.

## Materials and Methods

**Robophysical Experiments.** All of the robophysical models were designed in Solidworks and 3D-printed (LulzBot TAZ Workhorse) using PLA material. Each robot module has a pair of rigidly connected legs (12 cm in length). There are three servo motors (Robotis Dynamixel AX-12a) in each segment: One controls horizontal body bending and the other two control the fore/aft and up/down motion of the legs. Servo motors are powered with an external power supply (11.2 V) and communicate with the PC via a microcontroller (Robotis U2D2). During a single experiment, all gait parameters in the gait that the robot executes are constant, and servo motor set points are sent at a fixed frequency (33 Hz for the lowest robot speed, and 200 Hz for the highest speed). Each trial consisted on prescribing a desired gait and allowing the robot to traverse a terrain for 3 cycles. We performed a minimum of 5 and 10 trials in the homogeneous and heterogeneous terrain respectively.

To capture the position and orientation of the robot over time, we attached a reflective marker on each module of the robot over time and used an OptiTrack motion capture system (four Prime 17W cameras, capture frame rate of 360 frames per second, software: Motive) to track the positions of the markers in the workspace. The tracked data was analyzed in MATLAB.

**Gait Prescription of Multilegged Robots.** We use a binary variable  $c$  to represent the contact state of a leg, where  $c = 1$  represents the stance phase and  $c = 0$  represents the swing phase. Following (34), the contact pattern of symmetric quadrupedal gaits can be written as

$$\begin{aligned} c_l(\tau_c, 1) &= \begin{cases} 1, & \text{if } \mod(\tau_c, 2\pi) < 2\pi D \\ 0, & \text{otherwise} \end{cases} \\ c_l(\tau_c, i) &= c_l\left(\tau_c - 2\pi \frac{\xi}{n}(i-1), 1\right) \\ c_r(\tau_c, i) &= c_l(\tau_c + \pi, i), \end{aligned} \quad [7]$$

where  $\xi$  denotes the number of spatial waves on legs,  $D$  the duty factor, and  $c_l(\tau_c, i)$  ( $c_r(\tau_c, i)$ ) denotes the contact state of the  $i$ -th leg on the left (and the right) at gait phase  $\tau_c$ , and  $i \in \{1, \dots, n\}$  for  $2n$ -legged systems (SI Appendix, Fig. S1).

Legs generate self-propulsion by protracting during the stance phase to make contact with the environment and retracting during the swing phase to break contact. That is, the leg moves from the anterior to the posterior end during the stance phase and moves from the posterior to anterior end during the swing phase. With this in mind, we use a piece-wise sinusoidal function to prescribe the anterior/posterior excursion angles ( $\theta$ ) for a given gait phase ( $\tau_c$ ) defined earlier,

$$\begin{aligned} \theta_l(\tau_c, 1) &= \begin{cases} \Theta_{leg} \cos\left(\frac{\tau_c}{2D}\right), & \text{if } \mod(\tau_c, 2\pi) < 2\pi D \\ -\Theta_{leg} \cos\left(\frac{\tau_c - 2\pi D}{2(1-D)}\right), & \text{otherwise,} \end{cases} \\ \theta_l(\tau_c, i) &= \theta_l\left(\tau_c - 2\pi \frac{\xi}{n}(i-1), 1\right) \\ \theta_r(\tau_c, i) &= \theta_l(\tau_c + \pi, i), \end{aligned} \quad [8]$$

where  $\Theta_{leg}$  is the shoulder angle amplitude, and  $\theta_l(\tau_c, i)$  and  $\theta_r(\tau_c, i)$  denote the leg shoulder angle of the  $i$ -th left and right legs at gait phase  $\tau_c$ , respectively. Note that the shoulder angle is maximum ( $\theta = \Theta_{leg}$ ) at the transition from swing to the stance phase and is minimum ( $\theta = -\Theta_{leg}$ ) at the transition from the stance to swing phase. Note that we chose  $D = 0.5$  unless otherwise mentioned.

We then introduce lateral body undulation by propagating a wave along the backbone from head to tail. The body undulation wave is

$$\alpha(\tau_b, i) = \Theta_{body} \cos\left(\tau_b - 2\pi \frac{\xi^b}{n}(i-1)\right), \quad [9]$$

where  $\alpha(\tau_b, i)$  is the angle of  $i$ -th body joint at phase  $\tau_b$  and  $\xi^b$  denotes the number of spatial waves on the body. For simplicity, we assume that the number of spatial waves in body undulation and that in leg movement are the same, i.e.,  $\xi^b = \xi$ . In this way, gaits of multilegged locomotors, by superposition of a body wave and a leg wave, can be described as the phase of contact  $\phi_c$ , and the phase of lateral body undulation  $\tau_b$ . As discussed in ref. 34, the optimal body-leg coordination (optimal phasing of body undulation to assist leg retraction) is  $\phi_c = \tau_b - (\xi/N + 1/2)\pi$ .

**Dynamic Model.** As discussed in Eq. 2, the ground reaction force acting on the  $i$ -th module (a pair of legs and a body connection unit) is given by

$$f_y^i(\tau, v) = -\mu N \sin\left(\tan^{-1}\left(\frac{v_y(\tau, v)}{v_x(\tau)}\right)\right). \quad [10]$$

Thus, the total force acting on the  $n$ -link robot is

$$f_y^{all}(\tau, v) = -\mu N \sum_{i=0}^{n-1} \sin\left(\tan^{-1}\left(\frac{v_y(\tau + 2\pi \frac{\xi}{n}i, v)}{v_x(\tau + 2\pi \frac{\xi}{n}i)}\right)\right). \quad [11]$$

Now, we replace  $\tau$  as  $2\pi ft$  ( $t$  is time),  $N$  as  $mg/n$  ( $m$  is the mass of the robot), and  $f_y^{all}$  as  $-m\dot{v}$  and thus have

$$\hat{v}(t, v) = \frac{\mu g}{n} \sum_{i=0}^{n-1} \sin \left( \tan^{-1} \left( \frac{v_y (2\pi ft + 2\pi \frac{\xi}{n} i, v)}{v_x (2\pi ft + 2\pi \frac{\xi}{n} i)} \right) \right), \quad [12]$$

which we can solve numerically to get the dynamic simulation.

**Lego Field Setup.** We constructed an obstacle-rich environment using Lego blocks. First, we divided a 150-cm  $\times$  90-cm area of a wooden sheet into 1.5-cm  $\times$  1.5-cm squares (100 blocks along the length; 60 blocks along the width). The distributions of those Lego bricks<sup>#</sup> were generated by the MATLAB `rand()` function. Specifically, we used `rand()` to create a 100  $\times$  60 matrix with uniformly distributed random variables. We marked the row and column information for the entries with the highest 120 values. We placed the Lego bricks at the designated positions. Finally, we hot-glued Lego bricks on planned positions.

<sup>#</sup> Included in LEGO Classic Large Creative Brick Box: <https://www.lego.com/en-us/product/lego-large-creative-brick-box-10698>.

**Data, Materials, and Software Availability.** Code and recordings data have been deposited in Zenodo (<https://doi.org/10.5281/zenodo.7595514>; <https://doi.org/10.5281/zenodo.7595495>).

**ACKNOWLEDGMENTS.** We are grateful for funding from the NSF-Simons Southeast Center for Mathematics and Biology (Simons Foundation Autism Research Initiative Grant 594594), Army Research Office Grant W911NF-11-1-0514, and Army Research Office contract W911NF-19-1-0056; funding was also provided to D.I.G. by a Dunn Family Professorship.

Author affiliations: <sup>a</sup>Interdisciplinary Graduate Program in Quantitative Biosciences, Georgia Institute of Technology, Atlanta, GA 30332; <sup>b</sup>School of Physics, Georgia Institute of Technology, Atlanta, GA 30332; and <sup>c</sup>Institute for Robotics and Intelligent Machines, Georgia Institute of Technology, Atlanta, GA 30332

Author contributions: B.C., S.L., T.W., and D.I.G. designed research; B.C., J.H., and E.E. performed research; B.C., T.W., and D.S. contributed new reagents/analytic tools; B.C., J.H., and K.D. analyzed data; and B.C., S.L., E.E., K.D., T.W., D.S., and D.I.G. wrote the paper.

1. J. Gray, The mechanism of locomotion in snakes. *J. Exp. Biol.* **23**, 101–120 (1946).
2. B. C. Jayne, Kinematics of terrestrial snake locomotion. *Copeia* **1986**, 915–927 (1986).
3. J. J. Socha, Gliding flight in the paradise tree snake. *Nature* **418**, 603–604 (2002).
4. R. L. Hatton, H. Choset, Generating gaits for snake robots: Annealed chain fitting and keyframe wave extraction. *Auton. Rob.* **28**, 271–281 (2010).
5. H. Marvi, D. L. Hu, Friction enhancement in concertina locomotion of snakes. *J. R. Soc. Interface* **9**, 3067–3080 (2012).
6. S. Kern, P. Koumoutsakos, Simulations of optimized anguilliform swimming. *J. Exp. Biol.* **209**, 4841–4857 (2006).
7. S. Jung, *Caenorhabditis elegans* swimming in a saturated particulate system. *Phys. Fluids* **22**, 031903 (2010).
8. R. D. Maladen, Y. Ding, C. Li, D. I. Goldman, Undulatory swimming in sand: Subsurface locomotion of the sandfish lizard. *Science* **325**, 314–318 (2009).
9. P. E. Schiebel *et al.*, Mechanical diffraction reveals the role of passive dynamics in a slithering snake. *Proc. Natl. Acad. Sci. U.S.A.* **116**, 4798–4803 (2019).
10. P. E. Schiebel *et al.*, Mitigating memory effects during undulatory locomotion on hysteretic materials. *Elife* **9**, e51412 (2020).
11. C. Li, T. Zhang, D. I. Goldman, A terradynamics of legged locomotion on granular media. *Science* **339**, 1408–1412 (2013).
12. L. E. Becker, S. A. Koehler, H. A. Stone, On self-propulsion of micro-machines at low Reynolds number: Purcell's three-link swimmer. *J. Fluid Mech.* **490**, 15–35 (2003).
13. J. Avron, O. Gat, O. Kenneth, Optimal swimming at low Reynolds numbers. *Phys. Rev. Lett.* **93**, 186001 (2004).
14. D. Tam, A. E. Hosoi, Optimal stroke patterns for purcell's three-link swimmer. *Phys. Rev. Lett.* **98**, 068105 (2007).
15. H. C. Fu, T. R. Powers, C. W. Wolgemuth, Theory of swimming filaments in viscoelastic media. *Phys. Rev. Lett.* **99**, 258101 (2007).
16. D. Crowdny, S. Lee, O. Samson, E. Lauga, A. Hosoi, A two-dimensional model of low-Reynolds number swimming beneath a free surface. *J. Fluid Mech.* **681**, 24–47 (2011).
17. R. J. Full, D. E. Koditschek, Templates and anchors: Neuromechanical hypotheses of legged locomotion on land. *J. Exp. Biol.* **202**, 3325–3332 (1999).
18. B. Chong *et al.*, Frequency modulation of body waves to improve performance of sidewinding robots. *Int. J. Rob. Res.* **40**, 1547–1562 (2021).
19. H. C. Astley *et al.*, Modulation of orthogonal body waves enables high maneuverability in sidewinding locomotion. *Proc. Natl. Acad. Sci. U.S.A.* **112**, 6200–6205 (2015).
20. Y. Tanaka, K. Ito, T. Nakagaki, R. Kobayashi, Mechanics of peristaltic locomotion and role of anchoring. *J. R. Soc. Interface* **9**, 222–233 (2012).
21. A. DeSimone, F. Guarnieri, G. Noselli, A. Tatone, Crawlers, Crawlers in viscous environments: Linear vs. non-linear rheology. *Int. J. Nonlin. Mech.* **56**, 142–147 (2013).
22. J. Buchli, M. Kalakrishnan, M. Mistry, P. Pastor, S. Schaal, "Compliant quadruped locomotion over rough terrain" in 2009 IEEE/RSJ International Conference on Intelligent Robots and Systems (IEEE, 2009), pp. 814–820.
23. S. Kajita *et al.*, "Biped walking on a low friction floor" in 2004 IEEE/RSJ International Conference on Intelligent Robots and Systems (IROS) (IEEE Cat. No. 04CH37566) (IEEE, 2004), vol. 4, pp. 3546–3552.
24. A. J. Clark, T. E. Higham, Slipping, sliding and stability: Locomotor strategies for overcoming low-friction surfaces. *J. Exp. Biol.* **214**, 1369–1378 (2011).
25. D. S. Marigold, A. J. Bethune, A. E. Patla, Role of the unperturbed limb and arms in the reactive recovery response to an unexpected slip during locomotion. *J. Neurophysiol.* **89**, 1727–1737 (2003).
26. F. J. Elmer, Nonlinear dynamics of dry friction. *J. Phys. A: Math. General* **30**, 6057 (1997).
27. X. Zhou, C. Majidi, O. M. O'Reilly, Energy efficiency in friction-based locomotion mechanisms for soft and hard robots: Slower can be faster. *Nonlinear Dyn.* **78**, 2811–2821 (2014).
28. R. M. Alexander, *Locomotion of Animals* (Springer, 1982), vol. 163.
29. E. R. Westervelt, J. W. Grizzle, C. Chevallereau, J. H. Choi, B. Morris, *Feedback Control of Dynamic Bipedal Robot Locomotion* (CRC Press, 2018).
30. D. Zhao, S. Reven, Multi-legged steering and slipping with low DoF hexapod robots. *Bioinspiration Biomimetics* **15**, 045001 (2020).
31. B. Chong, T. Wang, E. Erickson, P. J. Bergmann, D. I. Goldman, Coordinating tiny limbs and long bodies: Geometric mechanics of lizard terrestrial swimming. *Proc. Natl. Acad. Sci. U.S.A.* **119**, e2118456119 (2022).
32. Y. O. Aydin, J. M. Rieser, C. M. Hubicki, W. Savoie, D. I. Goldman, "Physics approaches to natural locomotion: Every robot is an experiment" in *Robotic Systems and Autonomous Platforms* (Elsevier, 2019), pp. 109–127.
33. Y. Ozkan-Aydin, B. Chong, E. Aydin, D. I. Goldman, "A systematic approach to creating terrain-capable hybrid soft/hard myriapod robots" in 2020 3rd IEEE International Conference on Soft Robotics (RoboSoft) (IEEE, 2020), pp. 156–163.
34. B. Chong *et al.*, A general locomotion control framework for multi-legged locomotors. *Bioinspiration Biomimetics* **17**, 046015 (2022).
35. B. Chong *et al.*, Coordination of lateral body bending and leg movements for sprawled posture quadrupedal locomotion. *Int. J. Rob. Res.* **40**, 747–763 (2021).
36. H. C. Astley *et al.*, Surprising simplicities and syntheses in limbless self-propulsion in sand. *J. Exp. Biol.* **223**, jeb103564 (2020).
37. S. Berri, J. H. Boyle, M. Tasieri, I. A. Hope, N. Cohen, Forward locomotion of the nematode *C. elegans* is achieved through modulation of a single gait. *HFSR J.* **3**, 186–193 (2009).
38. L. Koens, E. Lauga, Rotation of slender swimmers in isotropic-drag media. *Phys. Rev. E* **93**, 043125 (2016).
39. F. Jing, S. Alben, Optimization of two-and three-link snakelike locomotion. *Phys. Rev. E* **87**, 022711 (2013).
40. S. Alben, Efficient sliding locomotion with isotropic friction. *Phys. Rev. E* **99**, 062402 (2019).
41. R. D. Maladen, Y. Ding, P. B. Umbanhauer, A. Kamor, D. I. Goldman, Mechanical models of sandfish locomotion reveal principles of high performance subsurface sand-swimming. *J. R. Soc. Interface* **8**, 1332–1345 (2011).
42. J. M. Rieser *et al.*, Geometric phase and dimensionality reduction in locomoting living systems. *arXiv [Preprint]* (2019). <http://arxiv.org/abs/1906.11374> (Accessed 23 February 2022).
43. S. Manton, The evolution of arthropodan locomotory mechanisms—part 3. The locomotion of the chilopoda and pauropoda. *Zool. J. Linnean Soc.* **42**, 118–167 (1952).
44. B. Anderson, J. Shultz, B. Jayne, Axial kinematics and muscle activity during terrestrial locomotion of the centipede *Scolopendra heros*. *J. Exp. Biol.* **198**, 1185–1195 (1995).
45. S. Dutta *et al.*, Programmable coupled oscillators for synchronized locomotion. *Nat. Commun.* **10**, 1–10 (2019).
46. S. Kuroda, N. Uchida, T. Nakagaki, Gait switching with phase reversal of locomotory waves in the centipede *Scolopocryptops rubiginosus*. *Bioinspiration Biomimetics* **17**, 026005 (2022).
47. K. Yasui, K. Sakai, T. Kano, D. Owaki, A. Ishiguro, Decentralized control scheme for myriapod robot inspired by adaptive and resilient centipede locomotion. *Plos One* **12**, e0171421 (2017).
48. K. Yasui *et al.*, Decoding the essential interplay between central and peripheral control in adaptive locomotion of amphibious centipedes. *Sci. Rep.* **9**, 1–11 (2019).
49. S. Aoi *et al.*, Advantage of straight walk instability in turning maneuver of multilegged locomotion: A robotics approach. *Sci. Rep.* **6**, 1–10 (2016).
50. C. T. Farley, C. R. Taylor, A mechanical trigger for the trot-gallop transition in horses. *Science* **253**, 306–308 (1991).
51. J. Gray, G. Hancock, The propulsion of sea-urchin spermatozoa. *J. Exp. Biol.* **32**, 802–814 (1955).
52. S. Alben, Efficient sliding locomotion of three-link bodies. *Phys. Rev. E* **103**, 042414 (2021).
53. R. D. Maladen, Y. Ding, P. B. Umbanhauer, A. Kamor, D. I. Goldman, Mechanical models of sandfish locomotion reveal principles of high performance subsurface sand-swimming. *J. R. Soc. Interface* **8**, 1332–1345 (2011).
54. D. L. Hu, J. Niroidy, T. Scott, M. J. Shelley, The mechanics of slithering locomotion. *Proc. Natl. Acad. Sci. U.S.A.* **106**, 10081–10085 (2009).
55. J. M. Rieser, T. D. Li, J. L. Tingle, D. I. Goldman, J. R. Mendelson III, Functional consequences of convergently evolved microscopic skin features on snake locomotion. *Proc. Natl. Acad. Sci. U.S.A.* **118**, e2018264118 (2021).
56. J. Gray, Undulatory propulsion. *J. Cell Sci.* **3**, 551–578 (1953).
57. B. C. Jayne, Muscular mechanisms of snake locomotion: An electromyographic study of lateral undulation of the Florida banded water snake (*Nerodia fasciata*) and the yellow rat snake (*Elaphe obsoleta*). *J. Morphol.* **197**, 159–181 (1988).
58. G. J. Stephens, B. Johnson-Kerner, W. Bialek, W. S. Ryu, Dimensionality and dynamics in the behavior of *C. elegans*. *PLoS Comput. Biol.* **4**, e1000028 (2008).
59. S. D. Kelly, R. M. Murray, Geometric phases and robotic locomotion. *J. Rob. Syst.* **12**, 417–431 (1995).
60. J. Ostrowski, J. Burdick, The geometric mechanics of undulatory robotic locomotion. *Int. J. Rob. Res.* **17**, 683–701 (1998).
61. A. Shapere, F. Wilczek, *Geometric Phases in Physics* (World Scientific, 1989).

62. R. L. Hatton, H. Choset, Nonconservativity and noncommutativity in locomotion. *Eur. Phys. J. Special Topics* **224**, 3141–3174 (2015).
63. E. A. Shammas, H. Choset, A. A. Rizzi, Geometric motion planning analysis for two classes of underactuated mechanical systems. *Int. J. Rob. Res.* **26**, 1043–1073 (2007).
64. R. L. Hatton, Y. Ding, H. Choset, D. I. Goldman, Geometric visualization of self-propulsion in a complex medium. *Phys. Rev. Lett.* **110**, 078101 (2013).
65. J. Hwangbo *et al.*, Learning agile and dynamic motor skills for legged robots. *Sci. Rob.* **4**, eaau5872 (2019).
66. J. Pratt, G. Pratt, "Intuitive control of a planar bipedal walking robot" in *Proceedings of 1998 IEEE International Conference on Robotics and Automation (Cat. No. 98CH36146)* (IEEE, 1998), vol. 3, pp. 2014–2021.
67. U. Saranli, M. Buehler, D. E. Koditschek, Rhex: A simple and highly mobile hexapod robot. *Int. J. Rob. Res.* **20**, 616–631 (2001).
68. A. A. Transeth, R. I. Leine, C. Glocker, K. Y. Pettersen, P. Liljeback, Snake robot obstacle-aided locomotion: Modeling, simulations, and experiments. *IEEE Trans. Rob.* **24**, 88–104 (2008).
69. T. Wang *et al.*, "The omega turn: A biologically-inspired turning strategy for elongated limbless robots" in *2020 IEEE/RSJ International Conference on Intelligent Robots and Systems (IROS)* (IEEE, 2020), pp. 7766–7771.
70. T. Wang *et al.*, "Generalized omega turn gait enables agile limbless robot turning in complex environments" in *2022 International Conference on Robotics and Automation (ICRA)* (IEEE, 2022), pp. 1–7.
71. Y. Ozkan-Aydin, D. I. Goldman, Self-reconfigurable multilegged robot swarms collectively accomplish challenging terrodynamic tasks. *Sci. Rob.* **6**, eabf1628 (2021).
72. S. Aoi, Y. Eguchi, K. Tsuchiya, Instability-based mechanism for body undulations in centipede locomotion. *Phys. Rev. E* **87**, 012717 (2013).